The Astrophysical Journal Letters, 997:L40 (15pp), 2026 February 1 https://doi.org/10.3847/2041-8213/ae36a1

Extreme Winds on the Emerging Dayside of an Ultrahot Jupiter

Yapeng Zhang[1,18], Joost P. Wardenier[2,3], Aaron Householder[4,5,19], Thaddeus D. Komacek[6], Aurora Y. Kesseli[7], Fei Dai[8], Andrew W. Howard[1], Julie Inglis[9], Howard Isaacson[10], Heather A. Knutson[9], Dimitri Mawet[1], Lorenzo Pino[11], Nicole Wallack[12], Jerry W. Xuan[1,13,18], Theron W. Carmichael[8,20], Daniel Huber[8], Rena A. Lee[8], Nicholas Saunders[14,15], Lauren Weiss[16], and Jingwen Zhang[8,17]

[1] Department of Astronomy, California Institute of Technology, Pasadena, CA 91125, USA
[2] Weltraumforschung und Planetologie, Physikalisches Institut, University of Bern, Gesellschaftsstrasse 6, 3012 Bern, Switzerland
[3] Institut Trottier de Recherche sur les Exoplanetes, Universite de Montreal, Montreal, Quebec, H3T 1J4, Canada
[4] Department of Earth, Atmospheric and Planetary Sciences, Massachusetts Institute of Technology, Cambridge, MA 02139, USA
[5] Kavli Institute for Astrophysics and Space Research, Massachusetts Institute of Technology, Cambridge, MA 02139, USA
[6] Department of Physics (Atmospheric, Oceanic and Planetary Physics), University of Oxford, Oxford, OX1 3PU, UK
[7] IPAC, Mail Code 100-22, Caltech, 1200 E. California Boulevard, Pasadena, CA 91125, USA
[8] Institute for Astronomy, University of Hawaií, 2680 Woodlawn Drive, Honolulu, HI 96822, USA
[9] Division of Geological & Planetary Sciences, California Institute of Technology, Pasadena, CA 91125, USA
[10] Department of Astronomy, University of California Berkeley, Berkeley, CA 94720, USA
[11] INAF—Osservatorio Astrofisico di Arcetri, Largo Enrico Fermi 5, I-50125 Firenze, Italy
[12] Earth and Planets Laboratory, Carnegie Institution for Science, Washington, DC, 20015, USA
[13] Department of Earth, Planetary, and Space Sciences, University of California, Los Angeles, CA 90095, USA
[14] Department of Astronomy, Yale University, New Haven, CT 06511, USA
[15] Institute for Astronomy, University of Hawaii at Mānoa, 2680 Woodlawn Drive, Honolulu, HI 96822, USA
[16] Department of Physics and Astronomy, University of Notre Dame, Notre Dame, IN, 46556, USA
[17] Department of Physics, University of California, Santa Barbara, CA 93106, USA
Received 2025 December 2; revised 2026 January 7; accepted 2026 January 9; published 2026 January 28

Abstract

High-resolution spectroscopy provides a unique opportunity to directly probe atmospheric dynamics by resolving Doppler shifts of planetary signals as a function of orbital phase. Using the optical spectrometer the Keck Planet Finder, we carry out a pilot study on high-resolution phase-curve spectra of the ultrahot Jupiter KELT-9 b. We spectrally and temporally resolve its dayside emission from posttransit to preeclipse (orbital phase $\phi = 0.1$–0.45). The signal strength and width increase with orbital phase as the dayside rotates into view. The net Doppler shift varies progressively from -13.4 ± 0.6 to $-0.4 \pm 1.0\,\mathrm{km\,s^{-1}}$, the extent of which exceeds its rotation velocity of $6.4 \pm 0.1\,\mathrm{km\,s^{-1}}$, providing unambiguous evidence of atmospheric winds. We devise a retrieval framework to fit the full time-series spectra, accounting for the variation of the line profiles due to the rotation and winds. We retrieve a supersonic day-to-night wind speed up to $11.7 \pm 0.6\,\mathrm{km\,s^{-1}}$ on the emerging dayside, representing the most extreme atmospheric winds in hot Jupiters to date. Comparison to 3D circulation models reveals weak atmospheric drag, consistent with relatively efficient heat recirculation, as also supported by space-based phase-curve measurements. Additionally, we retrieve the dayside chemistry (including Fe I, Fe II, Ti I, Ti II, Ca I, Ca II, Mg I, and Si I) and temperature structure, and we place constraints on the nightside thermal profile. Our high-resolution phase-curve spectra and the measured supersonic winds provide excellent benchmarks for extreme physics in circulation models, demonstrating the power of this technique in understanding the climates of hot Jupiters.

Unified Astronomy Thesaurus concepts: Exoplanet atmospheres (487); Exoplanet atmospheric dynamics (2307); High resolution spectroscopy (2096)

1. Introduction

Ultrahot Jupiters (UHJs), which represent the hottest class of close-in gas-giant exoplanets with orbital periods of less than a few days, are natural laboratories for investigating atmospheric physics under extreme conditions. UHJs are tidally locked and have extremely irradiated daysides with temperatures above 2200 K, leading to atomic species dominating the spectra (H. J. Hoeijmakers et al. 2018, 2019; V. Parmentier et al. 2018). Their dayside atmospheres are predicted to be cloud-free, with molecules being thermally dissociated (e.g., H_2O/OH) and atoms being further ionized (D. Kitzmann et al. 2018; J. D. Lothringer et al. 2018). As atomic metals, metal hydrides, and oxides are efficient absorbers at UV and optical wavelengths, significant heat is deposited in the upper atmospheres, resulting in inverted temperature structure as a function of pressure. The thermal inversion has been ubiquitously detected on the daysides of UHJs, showing spectral features in emission (e.g., L. Kreidberg et al. 2018; S. K. Nugroho et al. 2020; L. Pino et al. 2020; F. Yan et al. 2020). On the other hand, refractory species may condense out on the nightside and be incorporated into clouds (D. S. Spiegel et al. 2009). The extreme temperature and chemistry gradients across hemispheres make them interesting targets for investigating the 3D nature and atmospheric circulation of planets.

[18] 51 Pegasi b Fellow.
[19] NSF Graduate Research Fellow.
[20] NSF Ascend Postdoctoral Fellow.

Previous phase-curve observations with space telescopes such as Spitzer, TESS, and CHEOPS have enabled the mapping of the temperature distributions in hot-Jupiter atmospheres (e.g., H. A. Knutson et al. 2007; N. B. Cowan & E. Agol 2008). The interplay between various factors—including irradiation, molecular dissociation, disequilibrium chemistry, and magnetic effects—regulates the heat redistribution (T. J. Bell & N. B. Cowan 2018; X. Tan & T. D. Komacek 2019; H. Beltz et al. 2022). Generally, the UHJ population shows enhanced day-to-night temperature differences and hence smaller heat recirculation efficiencies compared to normal hot Jupiters (T. J. Bell et al. 2021; L. Dang et al. 2025). This has been explained by theoretical studies and general circulation models (GCMs), suggesting that the radiative heating/cooling and the frictional drag (due to turbulence or ionized atmospheres coupled to magnetic fields) can efficiently damp waves, leading to inefficient day-to-night heat transport at high-equilibrium temperatures (T. D. Komacek & A. P. Showman 2016; T. D. Komacek et al. 2017; H. Beltz et al. 2022; H. Beltz & E. Rauscher 2024). The different circulation patterns also display distinct winds and dynamical signatures. GCMs suggest a regime transition from zonal jets to global day-to-night flows with increasing irradiation and lower pressures (A. P. Showman et al. 2013; T. D. Komacek & A. P. Showman 2016). High-resolution spectroscopy can resolve the spectral features, providing a unique opportunity to directly measure atmospheric winds (I. Snellen 2025). Therefore, the characterization of dynamics with high-resolution spectroscopy forms a complementary and powerful approach to revealing atmospheric circulations in addition to space-based phase curves.

With the increased signal-to-noise ratio (S/N) enabled by the ensemble of high-resolution spectrographs ($\lambda/\Delta\lambda \sim$ 100,000) on large telescopes, temporally and spectrally resolving atmospheric features has recently become possible. Time-resolved transmission spectroscopy reveals asymmetric absorption signals between the dawn and dusk limbs of UHJs, such as WASP-76 b and WASP-121 b, which show absorption that is progressively blueshifted and gaining in amplitude during the transit (D. Ehrenreich et al. 2020; A. Y. Kesseli & I. A. G. Snellen 2021; J. P. Wardenier et al. 2024; B. Prinoth et al. 2025; J. V. Seidel et al. 2025). The temporal variations can be interpreted as consequences of day-to-night winds combined with spatial gradients in thermal structure, chemistry, or clouds between the daysides and nightsides. These observations have been extensively investigated with state-of-the-art GCMs and have led to key insights into the 3D structure of UHJs (J. P. Wardenier et al. 2021, 2024; H. Beltz et al. 2022; A. B. Savel et al. 2022; A. Y. Kesseli et al. 2024).

Although these transmission observations have been vital so far, the region of the atmosphere probed during transmission spectroscopy is limited to the terminators. Resolving planetary emission as a function of orbital phase angles provides critical information on thermal and dynamical structures across a wide range of longitudes. Previous high-resolution emission spectroscopy studies have explored the dayside orbital phases around secondary eclipses. M. K. Herman et al. (2022) and L. van Sluijs et al. (2023) reported asymmetric signal strengths between the pre- and posteclipse phases of WASP-33 b, likely as a result of an eastward hotspot offset. In contrast, L. Pino et al. (2022) and A. Ridden-Harper et al. (2023) found no evidence for variation of the amplitude of spectral lines with phase on the dayside of KELT-9 b. L. Pino et al. (2020) also investigated the Doppler shifts as a function of orbital phase to constrain the wind pattern. They detected a deviation between the Doppler shift of iron lines and the best-fit circular orbit solution of the planet, which they attribute to winds of several up to 10 km s^{-1}. They also study the phase dependence of the Doppler shift and favor day-to-night winds over an equatorial jet, but their conclusions on the geometry of winds remain tentative, due to the limited S/N.

On the modeling side, there are multiple studies that investigate phase-resolved emission spectra using GCMs, including J. Zhang et al. (2017), H. Beltz & E. Rauscher (2024), and J. P. Wardenier et al. (2025). These predict quasi-sinusoidal Doppler shifts as a function of orbital phase, driven by planet rotation. Different atmospheric drags or magnetic effects, showing various wind patterns, can lead to deviations from such curves (J. P. Wardenier et al. 2025). In particular, the most prominent Doppler shifts occur in phases before quadrature (orbital phase: $\phi \sim 0.05$–0.25), which are therefore the most diagnostic. Yet, no existing observations have high enough S/N and the phase coverage to conclusively constrain different GCM predictions.

In this Letter, we perform a case study on one of the most favorable emission targets, KELT-9 b, to resolve the planetary signal across a wide range of orbital phases and unveil its thermal structure and wind pattern. We present our observations and data reduction in Section 2. We perform cross-correlation and retrieval analysis to detect the planetary emission and constrain atmospheric properties. The model setup and analysis methods are described in Section 3. Then, Section 4 presents the detection and retrieval results. We discuss the comparison to GCMs and implications for the circulation and climate of KELT-9 b in Section 5. Finally, we summarize the findings in Section 6.

2. Observations and Data Reduction

KELT-9 b is the hottest exoplanet ($T_{\rm eq} \sim 4000$ K) discovered to date (B. S. Gaudi et al. 2017). It has a 1.48 days, nearly polar orbit around an A0 star (B. S. Gaudi et al. 2017; J. P. Ahlers et al. 2020). We summarize the literature studies on KELT-9 b in Appendix A. Here, we observed emission from KELT-9 b at multiple orbital phases with the Keck Planet Finder (KPF; S. R. Gibson et al. 2016, 2018, 2020b, 2024) on UT 2024 August 8, 20, and 27 (PI: Zhang). KPF is an echelle spectrometer that covers the optical wavelength range of 440–870 nm, with a spectral resolving power of $\mathcal{R}\sim$98,000. As the planet's orbital semiamplitude is high (>230 km s^{-1}), we choose an exposure time of 150 s, to limit the smearing of the signal within each exposure. During observations, the airmass varies from 1.07 to 1.7, and the average seeing condition ranges from 0.″3, on August 8, to 0.″5, on August 20 and 27. This delivers typical S/Ns per pixel of ∼400, 330, and 320 at 650 nm for each night, respectively. The total on-target times are 3.5 hr (84 exposures), 2.5 hr (59 exposures), and 5.2 hr (125 exposures) each night, respectively. The observations cover a wide range of orbital phases between $\phi = 0.05$–0.25 and $\phi = 0.30$–0.48, as illustrated in Figure 1.

We take the spectra extracted with the KPF Data Reduction Pipeline (DRP; S. R. Gibson et al. 2020b), which performs flat fielding, order tracing, and optimal extraction. The DRP achieves wavelength calibration with laser-frequency comb and thorium–argon exposures bracketing the science observations. We further

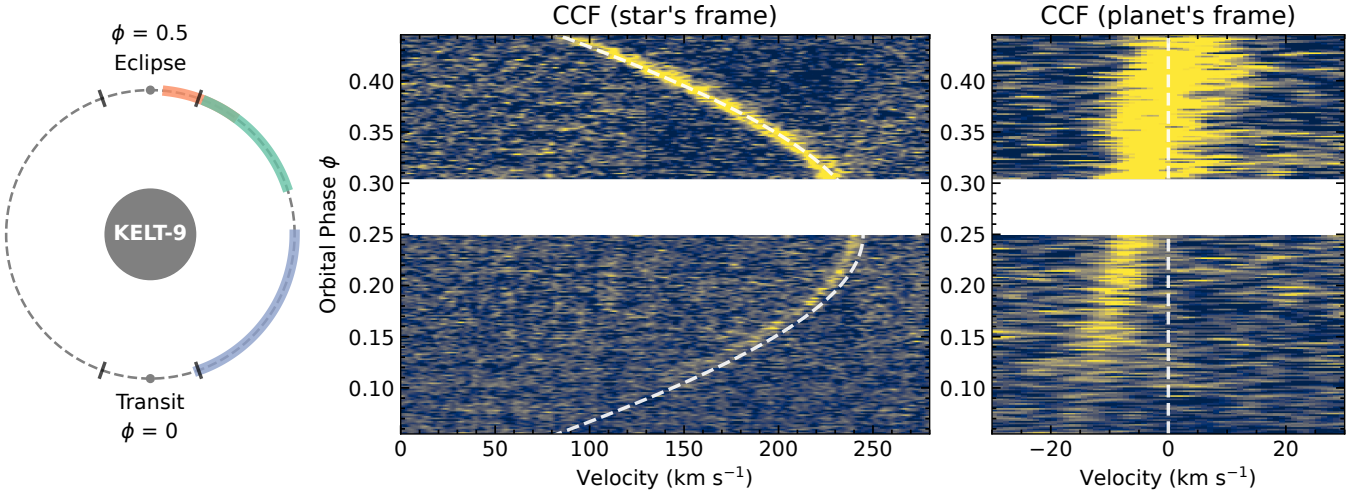

Figure 1. Detection of KELT-9 b's emission as a function of orbital phase. Left: the phase coverage of our KPF observations is shown by the three shaded curves. The black bars mark the timings of the transit and secondary eclipse. Middle: CCF map of the spectral data from posttransit to preeclipse in the star's rest frame. The planetary signal is shown as the bright yellow trace, following a sinusoidal function of phases (the white dashed line) due to the orbital motion. Right: CCF map shifted to the planet's rest frame, assuming an orbital semiamplitude of $K_p = 244.8$ km s^{-1} (i.e., the inferred K_p value from retrievals, as detailed in Section 4.1). The planetary emission profile shows clear variation with phase.

perform blaze correction, using the blaze functions extracted from the smooth lamp pattern (see A. Householder et al. 2025 for details). Then we correct for telluric absorption features caused mainly by H_2O and O_2 in the Earth's atmosphere, using the ESO sky tool `molecfit` (A. Smette et al. 2015). The details of the telluric correction can be found in Appendix B. After telluric correction, we shift the observations to the stellar rest frame, by correcting for the systemic and barycentric velocities and the star's reflex motion. The systemic velocity is measured from the cross-correlation of the combined stellar spectrum with a PHOENIX model (T. O. Husser et al. 2013) of $T_{\rm eff} = 10{,}000$ K. We fit a Gaussian profile to the cross-correlation function (CCF) and find the center with $v_{\rm sys} = -17.65 \pm 0.06$ km s^{-1}. We note that this is not the optimal approach for estimating the $v_{\rm sys}$ of the fast-rotating star. To account for the $v_{\rm sys}$ uncertainty, we add a free parameter $\Delta v_{\rm sys}$ in our following retrieval analysis, as detailed in Sections 3.3 and 4.1.

We normalize each spectrum with a third-order polynomial per spectral order and obtain a master stellar spectrum by average combining the time series. Then, individual exposures in the time series are divided by the master stellar spectrum, to remove the stellar features. Any remaining low-order trend in the continuum is further removed with a fifth-order polynomial. The noisy wavelength channels due to strong telluric contamination are masked by clipping outliers above 5σ. This leads to $\sim$1.2% of wavelength channels being masked. The observation uncertainties σ_0 are estimated from the standard deviation of the residuals per wavelength channel after removing the master stellar spectrum. Given the exquisite data quality, we avoid any additional detrending processing to ensure the planetary signal remains unaltered.

3. Method

3.1. Atmospheric Model

To perform cross-correlation and retrieval analysis, we build atmospheric models of KELT-9 b and generate synthetic spectra using the radiative transfer tool `petitRADTRANS` (`pRT`; P. Mollière et al. 2019). We use the analytical pressure–temperature (P-T) profile in radiative equilibrium from T. Guillot (2010), which involves three parameters: the atmospheric opacity in the infrared (IR) wavelengths $\kappa_{\rm IR}$, the ratio between the optical and IR opacity γ, the equilibrium temperature $T_{\rm eq}$. Given the temperature structure, equilibrium chemical abundances are calculated on the fly with `easychem` (E. Lei & P. Mollière 2025). Chemical equilibrium is expected in the lower atmosphere probed by emission spectroscopy, where the thermal rates dominate over stellar irradiation and advection. The calculation also takes into account the thermal ionization of neutral atoms, such as Mg, Ca, Si, Fe, Ti, and V. As chemical abundances are not the focus of this study, we fix the composition to solar metallicity [Fe/H] = 0, which is typically retrieved for refractories in UHJs (S. Gandhi et al. 2023; S. Pelletier et al. 2025). We note that the model did not account for the non–local thermodynamic equilibrium (NLTE) effects on the thermal structure and line formation (J. D. Turner et al. 2020; L. Fossati et al. 2021). However, the difference is expected to be small for metal emission lines originating from the lower atmosphere ($P > 10^{-4}$ bar).

We generate emission spectra using `pRT` with the line-by-line mode. We consider the continuum opacity sources of collision-induced absorption from H_2–H_2, H_2–He, and H^- bound–free and free–free absorption, as well as line opacities from Fe I, Fe II, Ti I, Ti II, Na I, Ca I, Ca II, Mg I, Si I, V I, and V II. The line opacity cross sections are computed from the `Kurucz` line lists (R. L. Kurucz 2018), using the Python package `pyROX`[21] (S. de Regt et al. 2025) for temperatures up to 9000 K, which is sufficient for the temperature range of KELT-9 b. To speed up the calculation, we downsample the original opacity tables of $\mathcal{R} = 10^6$ by a factor of 3. This downsampling factor has been benchmarked in high-resolution retrieval studies (J. W. Xuan et al. 2022; Y. Zhang et al. 2024). Then we apply instrument broadening, by convolving the model spectrum to the KPF spectral resolution of $\mathcal{R} = 98{,}000$ with a Gaussian kernel. The planet-to-star flux ratio is then computed by $(R_p/R_*)^2 F_p/F_*$, where we use a PHOENIX model of $T_{\rm eff} = 10{,}000$ K broadened by $v \sin i = 115$ km s^{-1} as the stellar spectrum. Finally, we remove the

[21] https://github.com/samderegt/pyROX

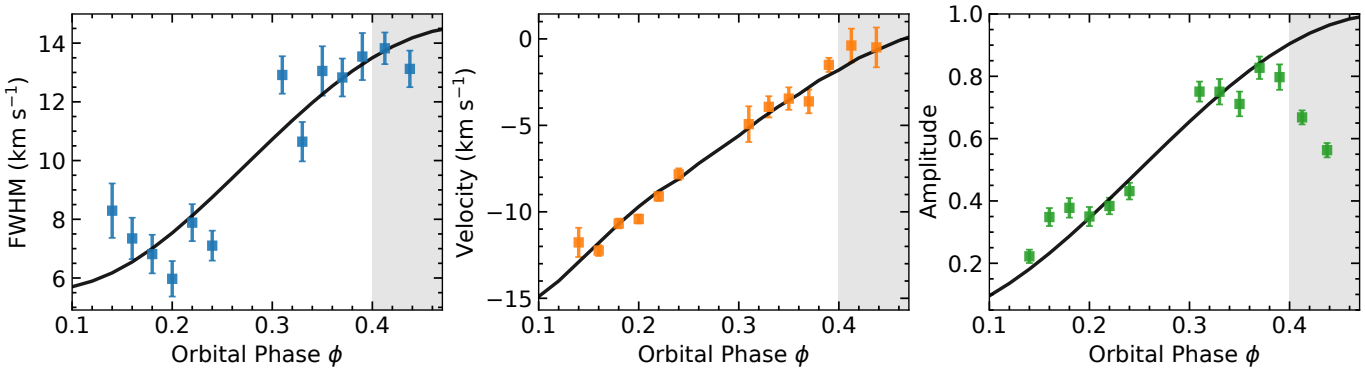

Figure 2. Phase dependency of the line width, net Doppler shift, and amplitude of KELT-9 b's emission signal, as extracted from the CCFs shown in Figure 1. The black lines represent the simple harmonic forms adopted in the retrieval analysis—see Equation (3) for the FWHM, Equation (2) for the amplitude, and Equation (4) for the net Doppler shift. The signal amplitude suffers from stellar contamination for $\phi > 0.4$ (gray shaded region).

continuum from the model, by subtracting the Gaussian-smoothed version with a kernel size of 150 pixels (∼2–4 Å).

3.2. Cross-correlation Analysis

We perform cross-correlation analysis to detect the planetary signal in the time-series spectra. The CCF is computed by

$$\mathrm{CCF}(v) = \boldsymbol{f}(v)^T \Sigma_0^{-1} \boldsymbol{y}, \quad (1)$$

where $\boldsymbol{f}(v)$ is the model template shifted to a given velocity v, Σ_0 is the covariance matrix with the diagonal items populated by the observation uncertainties σ_0, and $\boldsymbol{y}$ is the individual spectrum of the time-series observations. We calculate the CCF for a velocity range of $[-300, 300]$ km s^{-1} with a step of 1 km s^{-1}. We also compute the $v_{\rm sys}$–$K_{\rm p}$ diagram as commonly presented in the literature (M. Brogi et al. 2012). This is done by shifting the CCF time series to planet's rest frame, following $v_{\rm p} = K_{\rm p} \sin(2\pi\phi)$, and coadding them, assuming a range of $K_{\rm p}$ values from 0 to 350 km s^{-1}.

In the CCF map, we note a significant residual pattern caused by stellar pulsation (see Figure 10 in Appendix C), as also identified in previous light-curve and spectroscopic observations (I. Wong et al. 2020; A. Wyttenbach et al. 2020). The pulsation signal prominently contaminates the data within the velocity range of the stellar rotation $v \sin i \sim 115$ km s^{-1}. At most orbital phases, the planet's radial velocity (RV) is larger than this value, so the planetary signal is unaffected. However, the stellar contamination overlaps the planetary signal at $\phi < 0.1$ and $\phi > 0.4$, making the measured line strength and shape less reliable at those phases. For the visual clarity of the CCF map shown in Figure 1, we use the `tinygp`[22] package (D. Foreman-Mackey et al. 2024) to perform Gaussian Processes (GP) fitting to the CCFs within the velocity range of ±115 km s^{-1}, to remove the pulsation signal (A. Wyttenbach et al. 2020). We note that the contaminated phases are excluded for subsequent analyses, such as retrievals and phase-combined CCF detections.

3.3. Phase-resolved Retrieval Analysis

To retrieve the atmospheric properties of KELT-9 b, we carry out Bayesian inference analysis on the time-series observations. The large phase coverage presents challenges in fitting all spectra simultaneously, as the planetary emission varies significantly across orbital phases. On the other hand, it provides an excellent opportunity to reveal the 3D structure of the atmosphere. Inspired by previous emission studies and GCM results, we parameterize the phase dependency of the spectral features, including the line strength, width, and Doppler shift, using harmonic forms. Following M. K. Herman et al. (2022), A. Ridden-Harper et al. (2023), and H. J. Hoeijmakers et al. (2024), the line strength as a function of orbital phase assuming a uniform dayside and nightside is modeled as

$$A_{\rm p}(\phi) = 1 - C\cos^2(\pi(\phi - \theta)), \quad (2)$$

where C is the contrast factor between the dayside and nightside emissions in the form of $1 - F_{\rm night}/F_{\rm day}$, and θ is the phase offset of the peak emission. We fix $\theta = 0$, because our observations do not cover both pre- and posteclipse phases and are therefore less sensitive to this parameter. We fix $C = 1$ to consider the dayside contribution alone, i.e., $A_{\rm day} = 1 - \cos^2(\pi\phi)$. The nightside contribution is taken into account separately, with a $0.5 - \phi$ phase shift in Equation (2), which becomes $A_{\rm night} = 1 - \sin^2(\pi\phi)$. Although these are simplified prescriptions, the observed phase dependence of the amplitude matches well with this simple form, as shown in Figure 2. Here, we impose the phase-dependent scaling of the signal without any free parameters. In practice, any uncertainties related to the model amplitude will be effectively incorporated into the retrieved *P-T* profile.

Similarly, the phase variation of line widths is modeled as

$$\mathrm{FWHM}(\phi) = \omega \sin^2(\pi\phi), \quad (3)$$

where ω is the maximum line width when the dayside hemisphere is fully in view. This is informed by the GCM prediction (J. P. Wardenier et al. 2025), and the measured line widths from our observations also support this, as shown in Figure 2.

As for the net Doppler shift, its phase variation is mainly driven by the planet's rotation ($v_{\rm eq}$) and additional atmospheric winds. To describe winds flowing from the substellar point toward the nightside, we assume a simple sinusoidal dependence of longitudes, as $v_{\rm wind}(\varphi) = u_\varphi \sin\varphi$, where u_φ is the maximum zonal wind speed near terminators. This means that the wind is weak near the substellar point and reaches its maximum near the terminators. This prescription is

[22] https://github.com/dfm/tinygp

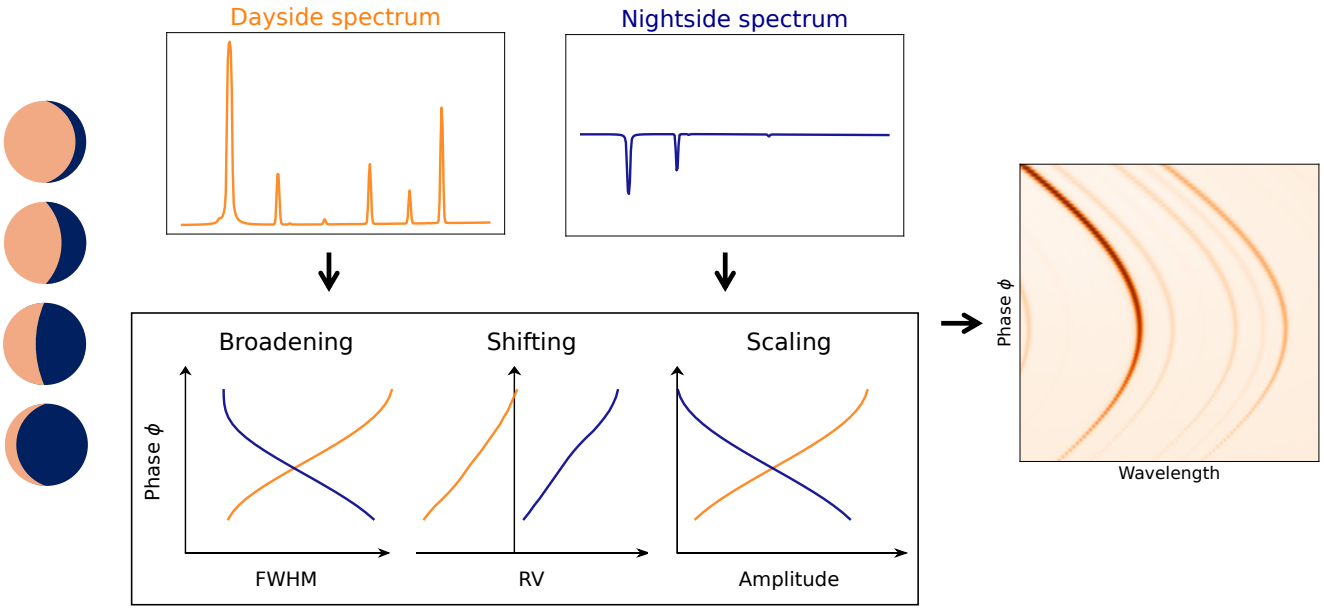

Figure 3. Illustration of the modeling framework for phase-resolved time-series spectra. With average dayside (thermal inversion; emission lines) and nightside (noninverted profile; absorption lines) spectra, we apply phase-dependent scaling, broadening, and Doppler shifting to model the full time-series observations.

motivated by the day-to-night flow pattern in GCM simulations (see Section 5.1 and Figure 11 in Appendix C). The line-of-sight velocity for each longitude (φ) and latitude (θ) location on the planet is given by

$$v_{\rm los}(\varphi, \theta) = (v_{\rm eq} + u_{\varphi} \sin\varphi)\sin(\phi + \varphi)\cos\theta, \quad (4)$$

where we neglect the meridional and vertical wind components (J. Zhang et al. 2017; L. Pino et al. 2022). The net Doppler shift is calculated by numerically integrating a single-line toy model in the visible hemisphere. We assume the same Gaussian line profile, with σ of 1 km s^{-1} (roughly the thermal broadening of Fe lines) but Doppler-shifted based on the $v_{\rm los}$ in each of the 192 × 94 pixelized patches on the planet's surface. At each orbital phase, we integrate the flux weighted by the projected surface area of each patch. The net Doppler shift is estimated from the peak location of the disk-integrated flux. We then apply this evaluated Doppler shift to the 1D model spectrum at each orbital phase.

This integration also provides the broadening of line profiles as a function orbital phase. However, it does not match the observed phase dependence of the FWHM, likely because of the simplified assumptions of no wind/turbulence dispersion and the identical line profile across different longitudes and latitudes. Therefore, we instead adopt the parametric form in Equation (3) for broadening our models. Future studies could improve the broadening prescription to better link it to the dynamical properties across the atmosphere.

With the atmospheric template as presented in Section 3.1, we apply the phase dependencies as described in Equations (2), (3), and (4) by scaling, broadening, and shifting the template according to each orbital phase to generate the time-series model. We account for the nightside emission by making a composite model that combines the dayside and nightside contributions. The nightside spectrum is also broadened, shifted, and scaled based on the opposite phase dependence ($0.5 - \phi$), as illustrated in Figure 3. This allows us to place tight constraints on the nightside thermal properties in the case of nondetection.

We exclude the orbital phases of $\phi < 0.11$ and $\phi > 0.4$ from the retrieval analysis, due to the stellar contamination, as mentioned in Section 3.2. We use data in all spectral orders, except for the two reddest orders with wavelengths from 848 to 870 nm covering the Ca II triplet. We note that the LTE models are not adequate for reproducing the strong and broad line shape of the Ca II triplet, which will be discussed separately in Section 4.2.

Then, we compare the model spectra to observations using the likelihood function from N. P. Gibson et al. (2020a; see also M. Brogi & M. R. Line 2019), as follows:

$$\ln\mathcal{L} = -\frac{N}{2}\ln\frac{\chi^2}{N} = -\frac{N}{2}\ln\left(\frac{1}{N}\sum_{i=1}^{N}\frac{(y_i - f_i)^2}{\sigma_i^2}\right), \quad (5)$$

which folds in the optimized scaling term β for observation uncertainties σ_i.

We assume uniform priors for the free parameters, including the temperature structure on the dayside and nightside, separately ($\kappa_{\rm IR}$, γ, and $T_{\rm eq}$), the orbital velocity $K_{\rm p}$, the offset from the systemic velocity $\Delta v_{\rm sys}$ to account for the measurement uncertainty of $v_{\rm sys}$, the maximum FWHM, and the wind speed u_{φ}. We use the nested sampling tool `PyMultiNest` (J. Buchner et al. 2014), which is a Python wrapper of the MultiNest method (F. Feroz et al. 2009), for the Bayesian inference. The retrievals are performed in importance nested sampling mode, with a constant efficiency of 5%. It uses 1000 live points to sample the parameter space and derives the posterior distribution of free parameters, as summarized in Table 1.

4. Results

4.1. From Phase-dependent Doppler Shifts to Winds

We present the CCF time series of KELT-9 b observations in Figure 1. To compute the CCFs, we use a static template (not broadened or shifted), as obtained from the best-fit model

Table 1
Priors and Posteriors of KELT-9 b Retrievals

Parameter	Prior	Posterior
K_p (km s^{-1})	$\mathcal{U}(200, 300)$	244.8 ± 1.2
Δv_{sys} (km s^{-1})	$\mathcal{U}(-10, 10)$	1.4 ± 0.9
u_φ (km s^{-1})	$\mathcal{U}(0, 20)$	11.7 ± 0.6
FWHM (km s^{-1})	$\mathcal{U}(5, 20)$	11.8 ± 0.5
T_{day} (K)	$\mathcal{U}(4000, 5000)$	4579 ± 120
T_{night} (K)	$\mathcal{U}(2000, 3000)$	...
$\log \kappa_{IR,day}$ (cm^2 g^{-1})	$\mathcal{U}(-5, -1)$	-4.42 ± 0.11
$\log \kappa_{IR,night}$ (cm^2 g^{-1})	$\mathcal{U}(-5, -1)$	>-3.2
$\log \gamma_{day}$	$\mathcal{U}(0, 3)$	0.61 ± 0.05
$\log \gamma_{night}$	$\mathcal{U}(-3, 0)$	>-0.9

Note. For the nondetected nightside emission, we include the 1σ lower limits for κ_{IR} and γ.

in the retrieval analysis (Section 3.3), which is further discussed in Section 4.2. The CCFs show a significant planetary detection across almost all orbital phases. In particular, we detect emission from the crescent dayside at posttransit phases ($\phi = 0.1$–0.25) for the first time. This extends the phase-resolved detection of UHJ emission to posttransit phases. In the star's rest frame, the planetary signal delineates a sinusoidal curve, as expected from the orbital motion $K_p \sin(2\pi\phi)$. We then correct for the orbital motion and shift the CCFs to the planet's rest frame, by assuming $K_p = 244.8$ km s^{-1}, which is inferred from retrievals, as discussed later in this section and shown in Figure 4. In the planet's rest frame, the signal shows a progressive blueshift from -0.4 ± 1.0 at $\phi \sim 0.45$ to -13.4 ± 0.6 km s^{-1} at $\phi \sim 0.1$. We measure the net Doppler shift as a function of orbital phase by fitting a Gaussian profile to the average CCF within every phase bin of 0.02. The phase dependences of the line widths, net Doppler shifts, and amplitudes are shown in Figure 2.

The RV shifts as a function of orbital phase are driven by the planet's rotation plus atmospheric winds. As the tidally locked planet rotates synchronously along with its orbital motion, it shows an increasing portion of the dayside hemisphere in view after the transit. This leads to a phase-dependent net Doppler shift of the disk-integrated emission relative to the planet's rest frame, because the flux is dominated by the dayside contribution. If there is no atmospheric dynamics, the signal is expected to follow a sinusoidal curve with a maximum blueshift at the level of the spin rate (J. Zhang et al. 2017; L. Pino et al. 2022; J. P. Wardenier et al. 2025). For KELT-9 b, the tidally locked spin rate corresponds to $v_{eq} = 6.4 \pm 0.1$ km s^{-1}, which is not sufficient for explaining the RV shift of 13 km s^{-1} observed at $\phi \sim 0.1$. Although any orbital eccentricity can also lead to the deviation of Doppler shifts from the assumed circular orbit, KELT-9 b shows no evidence of an eccentric orbit based on the TESS light curves ($e < 0.007$ at 2σ; I. Wong et al. 2020). This stringent upper limit on the eccentricity corresponds to a maximum RV deviation of $K_p e \sim 1.7$ km s^{-1}, which cannot account for the observed net Doppler shifts. We refer readers to L. Pino et al. (2022) for detailed discussion on the topic. Overall, this unambiguously suggests the presence of atmospheric winds that add to the Doppler shift induced by planet rotation.

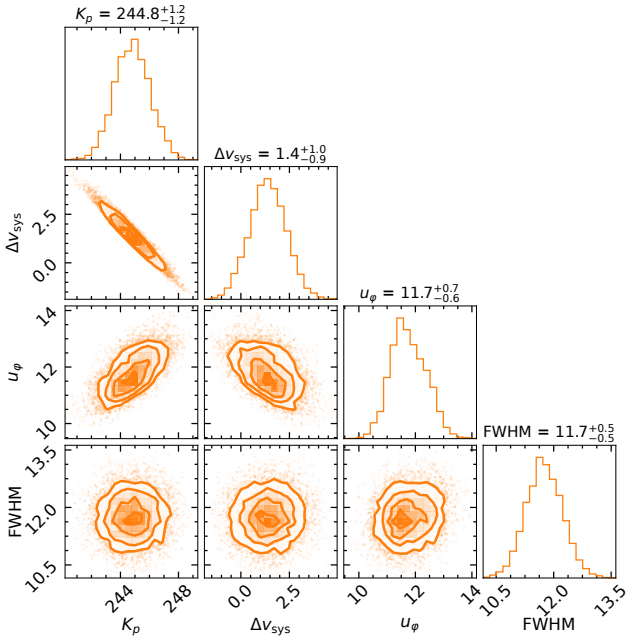

Figure 4. Corner plot of the retrieved orbital velocity K_p, systemic velocity offset Δv_{sys}, zonal wind speed u_φ, and line widths.

We test the impact of the uncertainties on the ephemeris, v_{sys}, and K_p on the measured net Doppler shifts. For the ephemeris, we propagate the uncertainties of the orbital period and transit midpoint (A. Kokori et al. 2023) to the phase calculation, which results in a maximum uncertainty of 0.3 km s^{-1} in RVs at individual orbital phases. This is much smaller than the resolution and line widths of the CCFs and hence negligible. For v_{sys}, the uncertainty only leads to a constant offset of the RVs, which does not affect the slope of the phase dependence, as shown in Figure 1. However, the uncertainty of K_p is critical in shaping the net RV trend across phases. The K_p values of KELT-9 b have large variations in the literature and therefore should be treated with caution. As pointed out in H. J. Hoeijmakers et al. (2024) and J. P. Wardenier et al. (2025), emission spectroscopy analyses are expected to result in a reduced K_p value compared to the true orbital velocity, due to the unaccounted-for effect of planet rotation, which essentially counteracts the orbital motion. Thanks to the large phase coverage of our observations, we can include the effect from planet rotation and atmospheric winds (Equation (4)) in retrievals and recover an accurate K_p as well as wind speeds. Using the parameterization described in Section 3.3, we retrieve the K_p and the maximum zonal wind u_φ from the phase-resolved observations, as shown in Figure 4 and Table 1. The marginalized values are $\Delta v_{sys} = 1.4 \pm 0.9$ km s^{-1}, $K_p = 244.8 \pm 1.2$ km s^{-1}, and $u_\varphi = 11.7 \pm 0.6$ km s^{-1}. This leads to a v_{sys} constraint of -16.2 ± 0.9 km s^{-1}. We note the negative correlation between v_{sys} and K_p, because our observations only cover the half orbit prior to the eclipse. Combining the observations with posteclipse phase coverage, which displays a positive v_{sys}–K_p correlation, will help to break the degeneracy and result in better constraints on these parameters.

Using the updated K_p, we estimate the stellar mass following H. J. Hoeijmakers et al. (2019). We obtain a revised stellar mass of $M_* = 2.26 \pm 0.03\, M_\odot$, a stellar radius of $R_* = 2.28 \pm 0.03\, R_\odot$, and a planet radius of

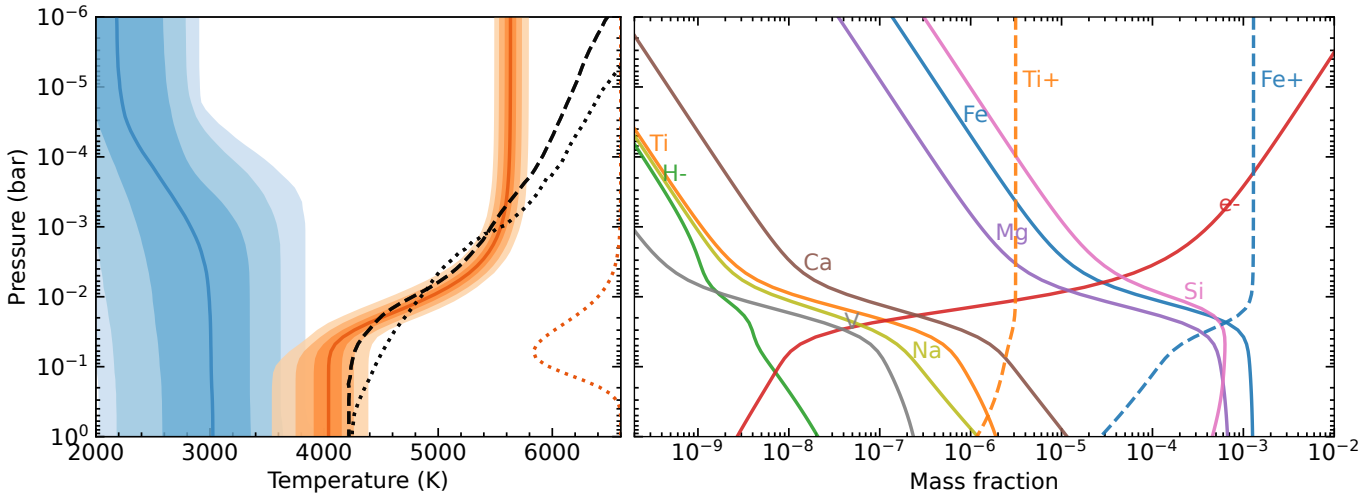

Figure 5. Left: retrieved *P-T* profiles of the dayside (orange) and nightside (blue). The dotted orange line shows the wavelength-averaged emission contribution as a function of pressure. The dashed and dotted black lines represent the self-consistent *P-T* profiles from J. D. Lothringer et al. (2018) and L. Fossati et al. (2021), for comparison. Right: equilibrium chemical abundance profiles for the mean dayside *P-T* structure.

$R_p = 1.82 \pm 0.03\,R_{\rm Jup}$, which uses the ρ_* and R_p/R_* values from B. S. Gaudi et al. (2017). Combining the RV amplitude K from A. Pai Asnodkar et al. (2022), the planet mass is then $M_p = 2.22 \pm 0.58\,M_{\rm Jup}$.

4.2. Thermal Structure and Chemistry

The retrieval analysis also provides constraints on the thermal structure of KELT-9 b. The retrieved *P-T* profile, with a strong temperature inversion on the dayside, is shown in Figure 5. It agrees well with self-consistent models for KELT-9 b (J. D. Lothringer et al. 2018; L. Fossati et al. 2021) in the pressure regimes probed by emission lines ($P \sim 10^{-4}$–10^{-1} bar, as shown by the emission contribution in Figure 5). We find similar results for pressures higher than 10^{-4} bar, while the lower-pressure regions are not well constrained by the observations. In addition, NLTE effects are expected to be significant in the upper atmospheres, leading to unreliable results with our LTE retrievals.

According to phase-curve measurements, the nightside temperature of KELT-9 b is estimated to be ∼2500–3000 K (M. Mansfield et al. 2020; I. Wong et al. 2020; K. Jones et al. 2022). This temperature is high enough to keep the metal species in gaseous form, and hence we expect the nightside to show absorption spectral features (because of noninverted *P-T* profiles) that the high-resolution observations are still sensitive to. However, we obtain a nondetection of the nightside emission with our KPF observations. Our retrieval with a composite dayside-and-nightside model places an upper limit on the nightside thermal structure, as shown in Figure 5. This nondetection implies a shallow vertical temperature gradient on the nightside. We can rule out large temperature gradients, as suggested by the γ parameter (Table 1). We plot an example of the fitted nightside spectrum model in Figure 9 in Appendix C for a visual comparison of the line strengths to those of the dayside emission spectrum. This suggests that the nightside line strength is over an order of magnitude smaller than the dayside signal, again highlighting the challenge of detecting nightside emission (J. P. Wardenier et al. 2025). Our temperature constraint is consistent with the nightside *P-T* profiles from the GCMs presented in M. Mansfield et al. (2020). However, the observations are not sensitive enough to distinguish the nightside thermal profiles predicted for different levels of atmospheric drag. Weak drag would lead to efficient heat redistribution and therefore relatively isothermal *P-T* profiles on the nightside, while strong drag means that the nightside is dominated by radiative processes and retains a cooler upper atmosphere. Upcoming JWST phase-curve observations will provide better insights into the nightside structure (K. Stevenson et al. 2025).

Regarding the chemical composition, we detect emission from Fe I, Fe II, Ti I, Ti II, Ca I, Ca II, Mg I, and Si I on the dayside. The mass fractions of these species in chemical equilibrium are shown in Figure 5. The onset of the thermal ionization of neutral metals occurs near the photosphere ($P \sim 10^{-2}$–10^{-1} bar) and dominates the chemistry at lower pressures. We present the CCF detections for individual species in Figure 6. The template for the individual species used in the cross-correlation is built from the retrieved best-fit model minus the contributions from all other species except the one being analyzed, as shown in Figure 9 in Appendix C. To assess the observational deviation from the chemical equilibrium model, we compare the observed average CCFs with the modeled CCFs, as shown in the bottom panels of Figure 6. The model shows generally good agreement with the observations, while underestimating the emission strength of Fe II and Ti I and overestimating the Si I signal. A similar underestimation of the Fe II signal has been reported in transmission studies as well (H. J. Hoeijmakers et al. 2019). The discrepancy is likely caused by NLTE effects, the nonequilibrium chemistry (e.g., photoionization), and the nonhydrostatic structure in the upper atmosphere.

We explore the potential velocity discrepancy across different species in Figure 6. The CCF peak locations are consistent for all neutral species, while the peak for ionized species tends to shift to a lower $K_{\rm p}$ and higher $v_{\rm sys}$. To quantify the velocity difference, we carry out a retrieval with separated wind speed parameters for neutral (e.g., Fe I and Ti I, etc.) and ionized species (e.g., Fe II and Ti II), respectively. We find consistent values for the two retrieved u_φ and therefore no clear evidence of different dynamical behaviors for ions versus neutrals. Instead, the differential velocity shifts are expected to be more prominent in atomic gases (e.g., H I, Na I, and Ca II) that probe distinct pressure levels or molecular species (e.g.,

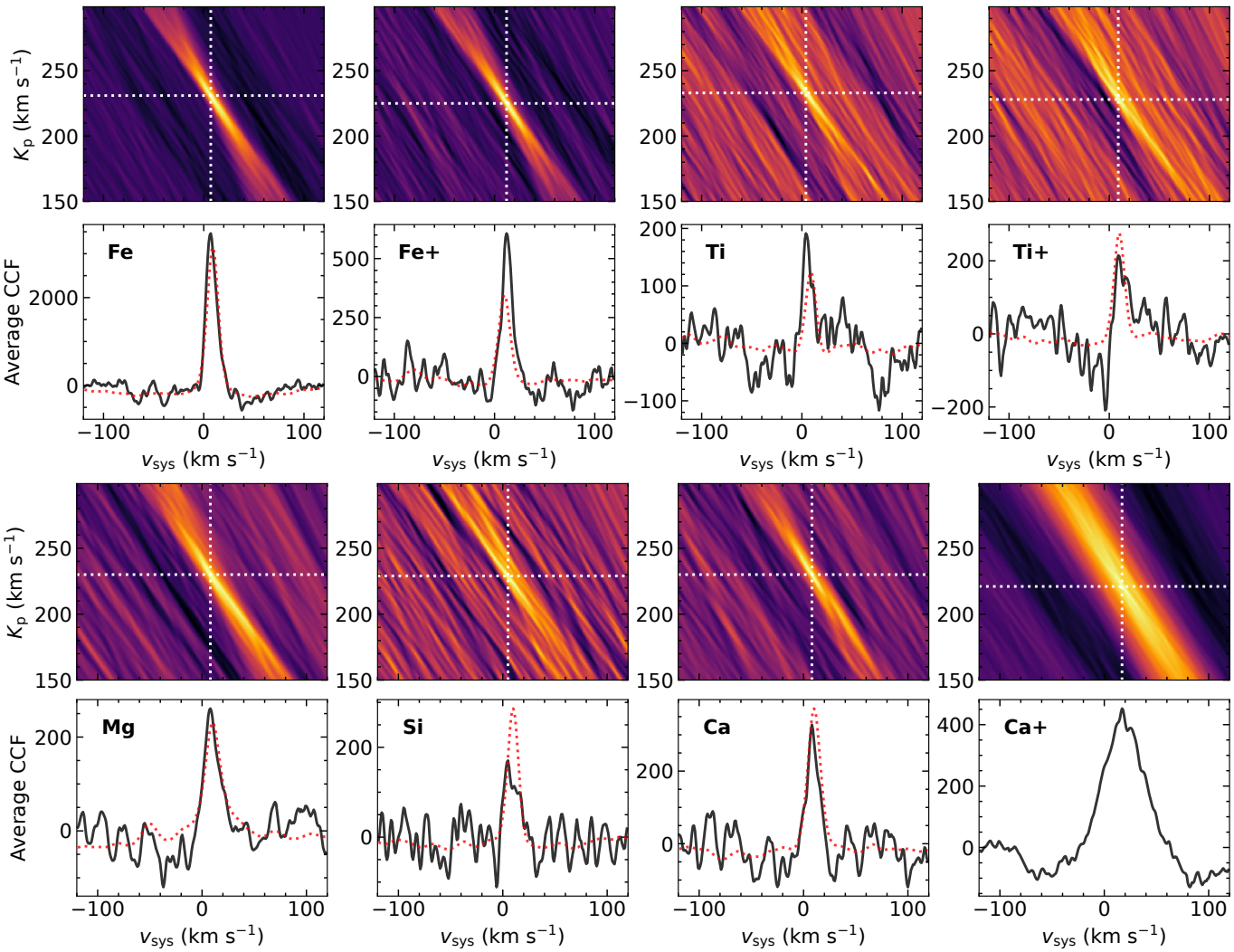

Figure 6. v_{sys}–K_p diagrams and average 1D CCF detections of Fe I, Fe II, Ti I, Ti II, Mg I, Si I, Ca I, and Ca II. The white dotted lines mark the locations of the CCF peaks. The red dotted lines show the model predictions of CCF signals.

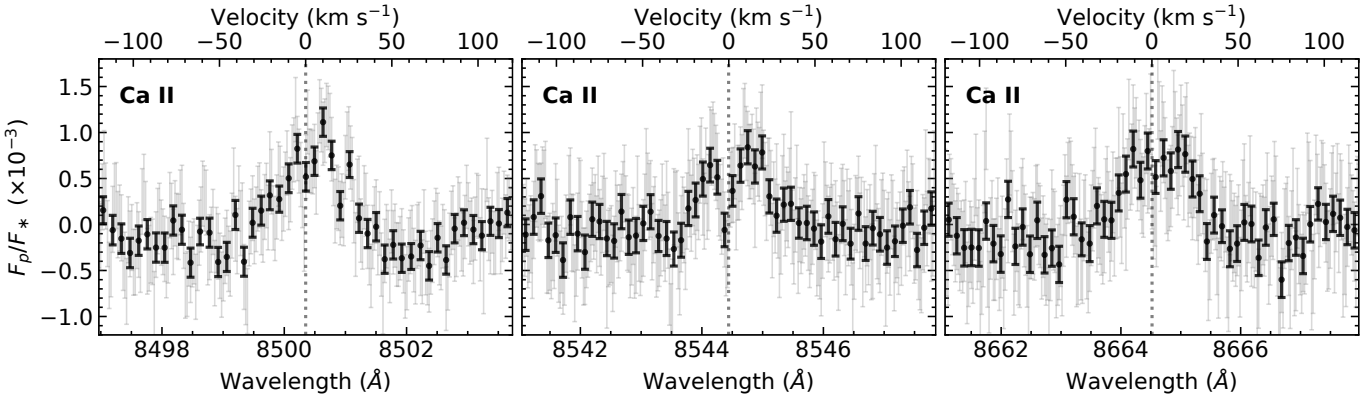

Figure 7. Resolved emission from Ca II triplet lines at 8500, 8544, and 8564 Å in KELT-9 b. The black data points represent the binned data for every 5 pixels of the original data (in gray).

H_2O and OH) that show spatial gradients due to dissociation (A. Y. Kesseli et al. 2022; M. Brogi et al. 2023; J. P. Wardenier et al. 2024; J. V. Seidel et al. 2025).

We resolve individual lines of the Ca II triplet at 8500.3, 8544.4, and 8664.5 Å, as shown in Figure 7. The broadening of the triplet (FWHM ~ 45 km s^{-1}) is significantly larger than that of other metal lines, indicating a distinct thermal and dynamical regime (Y. Zhang et al. 2022). We note that the wavelengths near the Ca II lines are excluded from the aforementioned retrieval analysis, because the lines originate from a higher region of the atmosphere where NLTE and hydrodynamical effects play significant roles and cannot be readily modeled with our framework. We encourage future studies to perform NLTE modeling on the Ca II triplet,

combining emission with transmission observations (F. Yan et al. 2019; N. W. Borsato et al. 2023; M. C. D'Arpa et al. 2024), which are particularly constraining on the thermal structure and dynamics in the upper atmosphere.

5. Discussion

5.1. Comparison to GCMs

To investigate the implications of the phase-dependent Doppler shifts on atmospheric dynamics, we compare our observations to the predictions from GCMs (X. Tan & T. D. Komacek 2019) for KELT-9 b, as presented in M. Mansfield et al. (2020). The model uses the double-gray approximation in the radiative transfer calculation, with wavelength-independent opacities within the visible and IR bands. As the double-gray assumption does not apply at low pressures, because the solution converges to an isotherm (E. Rauscher & K. Menou 2012), the model top boundary was cut at 1 mbar. This pressure range is sufficient, because our emission observations mainly probe pressures of 10^{-1}–10^{-3} bar, as shown in Figure 5. The GCMs include the cooling and heating effects due to the dissociation and recombination of molecular hydrogen, which are suggested to be critical for heat redistribution in UHJs (T. J. Bell & N. B. Cowan 2018). We use multiple GCMs with different levels of frictional drag, parameterized by a single drag timescale $\tau_{\rm drag}$, which is used to represent the effects of the magnetic field and turbulence in the linear regime. We consider $\tau_{\rm drag} = 10^3$ and 10^7 s, ranging from strong to weak drag. The simulations predict various strengths of the day-to-night flows at 10^{-2} bar, subject to the atmospheric drag. Weak drag can result in locally supersonic wind speeds up to 15 km s^{-1}, while strong drag can slow down the wind speed to 3 km s^{-1}.

We postprocess the outputs of the GCMs with the 3D Monte Carlo radiative transfer code gCMCRT (E. K. H. Lee et al. 2022), to simulate emission spectra at a range of orbital phases, from 0 to 0.5. We refer readers to J. P. Wardenier et al. (2025) for a detailed description of the code. We obtain a static dayside template by zeroing out any dynamical effects, then cross-correlating it with the simulated time-series spectra. The CCF maps as a function of orbital phase are shown in Figure 8. We note the similarly slanted traces in the simulated CCFs and observations (Figure 1), which are driven by planet rotation and winds (J. Zhang et al. 2017; J. P. Wardenier et al. 2025). Various levels of atmospheric drag can affect the wind pattern, therefore resulting in different phase dependences of the net Doppler shift. Figure 8 shows the phase variation of the CCF peak velocities for different drag timescales. The extracted net RVs from the observations are also shown for comparison. The observations match the $\tau_{\rm drag} = 10^7$ s model best. The strong day-to-night wind predicted in this weak-drag model is necessary to account for the large blueshifts ($\sim$13 km s^{-1}) seen in the observations.

Although the phase dependence of the net Doppler shifts can be generally reproduced by the GCMs, we caution that inferring accurate atmospheric drag from these models remains difficult. As a result of the double-gray approximation and the limited temperature range of opacity tables, these GCMs are unable to match the strong dayside thermal inversion from our retrievals. It is unclear how the underestimated dayside temperature would affect the wind structure. Future 3D modeling studies are needed to reassess the approximations and produce more realistic predictions. Our high-resolution phase-curve observations serve as valuable benchmarks for GCMs.

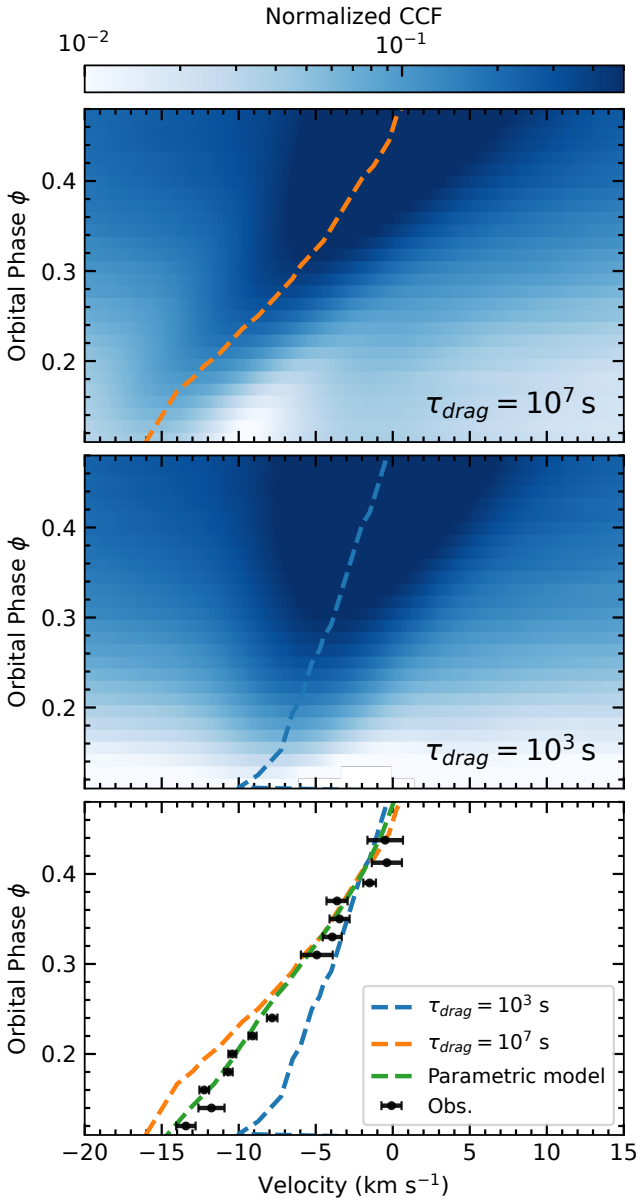

Figure 8. Net Doppler shifts of the planetary emission as a function of orbital phase compared to GCM predictions. Top and middle: predicted CCF maps for GCMs with different drag timescales—weak drag $\tau_{\rm drag} = 10^7$ s and strong drag $\tau_{\rm drag} = 10^3$ s. The dashed lines mark the locations of the CCF peaks at each orbital phase. Bottom: comparison of the phase–velocity trend between the observations and GCMs. The black data points are the measured velocities of the line centers, as also shown in Figure 2. The observations prefer the GCM with $\tau_{\rm drag} = 10^7$ s. The green dashed line shows the retrieved best-fit wind model with $u_\varphi = 11.7$ km s^{-1}.

Inspecting the GCM results, we find that the zonal winds across the dayside hemisphere can be well described by a sinusoidal function of longitude, as shown in Figure 11 in Appendix C. This supports our parameterization of the winds in Equation (4), allowing us to retrieve meaningful wind speeds directly from the observations. Independent from the GCMs, our retrieved wind speed of $u_\varphi = 11.7 \pm 0.6$ km s^{-1} is consistent with the GCM prediction with a drag timescale of $\tau_{\rm drag} \sim 10^7$ s. The day-to-night flow becomes supersonic near

the terminator regions, leading to blueshifts up to ~ -10 km s^{-1}, as also observed in transmission spectroscopy (A. P. Asnodkar et al. 2022; M. C. D'Arpa et al. 2024; M. Stangret et al. 2024). In parallel, the phase-curve measurements suggest a relatively small day-to-night temperature contrast and therefore an efficient heat redistribution in KELT-9 b, which can be attributed to molecular hydrogen dissociation and recombination (T. J. Bell & N. B. Cowan 2018; M. Mansfield et al. 2020; I. Wong et al. 2020). Both the thermal phase curve and the high-resolution Doppler measurements indicate a consistent picture of weak atmospheric drag, vigorous circulation, and strong day-to-night flows in KELT-9 b.

Supersonic winds are commonly predicted by models solving for hydrostatic primitive equations and filtering out sound waves, as presented here. More complex hydrodynamic Navier–Stokes models that allow for shocks also predict supersonic equatorial jets in hot Jupiters, despite showing $\sim$15% velocity fluctuations due to the Kelvin–Helmholtz instability (S. Fromang et al. 2016). Therefore, it is possible that KELT-9 b can maintain locally supersonic winds and display some variability in velocity. However, future modeling studies in the ultrahot regime of KELT-9 b are needed to understand the potential differences between hydrostatic and hydrodynamic models under such extreme conditions. The excellent data quality in this Letter provides the best opportunity to date to benchmark these GCMs.

5.2. Magnetic Fields

Constraints on the atmospheric drag can be useful for understanding the fundamental properties of UHJs that drive the atmospheric dynamics. In our GCMs, the atmospheric drag is parameterized as a Rayleigh drag force, characterized by a single timescale $\tau_{\rm drag}$ throughout the planet. Under this assumption, we can link the drag timescale to the magnetic field strength, following R. Perna et al. (2010) and J. Arcangeli et al. (2019):

$$\tau_{\rm drag} \sim \frac{4\pi\rho\eta}{B^2\cos\theta}, \tag{6}$$

where ρ is the density of the atmosphere, η is the magnetic diffusivity related to the ionization fraction (n_e), B is the magnetic field strength, and θ is the angle between the magnetic field and the flow direction. We estimate that a drag timescale of $\tau_{\rm drag} \sim 10^7$ s corresponds to a dipole magnetic field strength of $B_{\rm dip} \sim 3 \times 10^{-3}$ G, assuming a maximum efficiency ($\theta = 0$). This does not account for the direction dependence and spatially inhomogeneous strengths of the magnetic drag (E. Rauscher & K. Menou 2012; K. Batygin et al. 2013).

There seems to be a slight tension between the inferred weak magnetic drag and the expected strong B fields in this highly irradiated atmosphere. However, we caution that the simplified assumptions are likely invalid for the extreme atmosphere of KELT-9 b. The Rayleigh drag assumption only holds in the limit of a small magnetic Reynolds number $R_m = u_\varphi H/\eta < 1$, where u_ϕ is the zonal wind speed and H is the scale height. We estimate KELT-9 b to be in the high-magnetic-Reynolds-number regime of $R_m \sim 10^5$. In this nonlinear regime, the magnetic field can change the strength and direction of the Lorentz force in a time-dependent manner, leading to either the acceleration or deceleration of winds (T. M. Rogers & T. D. Komacek 2014; A. W. Hindle et al. 2021; W. Dietrich et al. 2022). Therefore, magnetohydrodynamic models are required to better assess the impacts of magnetic fields on the atmospheric dynamics (H. Beltz et al. 2022; H. Beltz & E. Rauscher 2024; A. Y. Kesseli et al. 2024). However, this has been challenging for the ultrahot regime of KELT-9 b, due to numerical limitations.

Alternatively, A. B. Savel et al. (2024) propose to constrain the magnetic field strength using differential wind velocities between heavy ions and neutral atoms in transmission, as the ionized gas is more strongly coupled to the magnetic field. However, emission observations probe higher pressure levels ($>$1 mbar), where the ion–neutral velocity difference due to magnetic effects is expected to be negligible (A. B. Savel et al. 2024). This is supported by the consistent winds inferred from neutral and ionized species, as discussed in Section 4.2.

5.3. Atmospheric Winds in the UHJ Population

Most previous studies of hot Jupiters have used high-resolution transmission spectroscopy to constrain atmospheric winds and have found that blueshifted absorption features appear to be ubiquitous in these observations (see the review in I. Snellen 2025). WASP-76 b and WASP-121 b represent the most favorable transmission targets with phase-resolved observations, displaying significant blueshifted atomic absorptions of up to 10 km s^{-1} toward the ends of the transits (D. Ehrenreich et al. 2020; F. Borsa et al. 2021b; A. Y. Kesseli & I. A. G. Snellen 2021). These blueshifts correspond to day-to-night wind speeds of $\sim$6.9 km s^{-1} for WASP-76 b and 5.6 km s^{-1} for WASP-121 b, as retrieved by S. Gandhi et al. (2023). WASP-172 b is inferred to show winds up to 10–14 km s^{-1}, based on the blueshifts of the Na doublet lines (J. V. Seidel et al. 2023). Moreover, different atoms and molecules tracing different pressures or longitudes exhibit distinct phase dependencies in transmission signals (J. P. Wardenier et al. 2024; J. V. Seidel et al. 2025), unlocking information on the 3D structures. In addition, dayside measurements also probe dynamical signatures. Using the redshifted dayside emission of CO and Fe, F. Lesjak et al. (2025) constrain a day-to-night wind velocity of $\sim$4.4 km s^{-1} for WASP-189 b. In contrast, A. R. Costa Silva et al. (2024) report blueshifted (-4.7 ± 0.3 km s^{-1}) Fe I emission on the dayside of WASP-76 b and propose that this can be caused by the material upwelling from the hotspot. In contrast, a recent study by G. Guilluy et al. (2025) contests the previous measurements and finds no blueshift along the $v_{\rm sys}$ axis but a negative shift in $K_{\rm p}$, in line with the predictions from J. P. Wardenier et al. (2025). Comparing winds at different UHJs has been challenging, due to the inhomogeneity of these diverse measurements.

For many UHJs, this picture is additionally complicated by their fast-rotating early-type host stars, which make it difficult to accurately measure $K_{\rm p}$ and $v_{\rm sys}$, hindering robust constraints on atmospheric dynamics. Different treatments of $K_{\rm p}$ in fitting can lead to contrary conclusions on the presence of winds (B. Prinoth et al. 2022, 2023, 2024). For atomic species, the stellar pulsation, Rossiter–McLaughlin effect, and center-to-limb variation can introduce contamination to the planetary transmission signals, making this approach less effective for many UHJs.

Our high-resolution phase-curve study suggests an alternative way of measuring winds that circumvents these systematics. The resolved phase dependence of the emission-line profiles helps to break the degeneracy between orbital motion and atmospheric dynamics, as we essentially rely on the relative Doppler shifts across a wide range of phases, which can be robustly measured despite the uncertainties in absolute values. In comparison to high-resolution transmission spectroscopy, emission observations trace the lower atmospheric region, where the hydrostatic and LTE assumptions are more valid, therefore making them better for benchmarking GCMs and revealing the underlying physics.

Despite these uncertainties, our new observations strongly suggest that KELT-9 b has the strongest day-to-night winds ($\sim$12 km s^{-1}) measured for an UHJ to date, consistent with its uniquely high irradiation. It is interesting to put this measurement into context at the population level. Do hotter planets always develop stronger winds? How does the wind speed correlate with planet properties such as the irradiation temperature, day-to-night contrast, heat recirculation efficiency, and magnetic strength? These questions call for extending such studies to more UHJs using the suite of high-resolution instruments, such as Keck/KPF (S. R. Gibson et al. 2020b), Keck/HISPEC (D. Mawet et al. 2019), Very Large Telescope (VLT)/ESPRESSO (F. Pepe et al. 2021), VLT/CRIRES+ (R. J. Dorn et al. 2023), GEMINI/MAROON-X (A. Seifahrt et al. 2018), and GEMINI/IGRINS-2 (H. Oh et al. 2024), etc. Combined with space-based phase-curve measurements (D. K. Sing et al. 2024), these observations will soon unveil trends in atmospheric dynamics with planet properties and constrain the driving mechanisms behind these trends in UHJs. This will in turn open up a novel window into the wind patterns of canonical hot Jupiters in the era of Extremely Large Telescopes.

6. Conclusion

We characterize the atmosphere of the UHJ KELT-9 b using phase-resolved emission spectroscopy with KPF ($\mathcal{R}\sim$98,000) in optical wavelengths. The observations cover a wide range of orbital phases, from 0.05 to 0.48, and result in the detection of planetary dayside emission throughout the half orbit from posttransit to preeclipse. Our findings are summarized as follows.

1. We resolve the planetary emission at posttransit phases ($\phi = 0.1$–0.25) under high spectral resolution for the first time.
2. The temporally resolved emission signals show phase-dependent profiles in terms of line strengths, widths, and Doppler shifts. The net Doppler shift varies progressively from -13.4 ± 0.6 to -0.4 ± 1.0 km s^{-1}, unambiguously driven by planet rotation plus atmospheric winds.
3. We parameterize the phase variations of line profiles and perform retrieval analysis on the full dataset of the high-resolution phase-curve observations. We retrieve the thermally inverted dayside vertical temperature profile and place an upper limit on the nightside thermal structure.
4. The retrieval reveals a supersonic day-to-night wind speed up to 11.7 ± 0.6 km s^{-1} on the emerging dayside of KELT-9 b, representing the most extreme atmospheric winds at hot Jupiters to date.
5. We report cross-correlation detections of atomic species, including Fe I, Fe II, Ti I, Ti II, Ca I, Ca II, Mg I, and Si I, on the dayside.
6. We run 3D radiative transfer on double-gray GCM outputs to simulate the phase variation of the high-resolution emission spectra. The comparison to GCMs points toward weak atmospheric drag, consistent with the retrieved strong wind speed ($\sim$12 km s^{-1}). This also agrees with the photometric phase curves, which suggest high temperature ($\sim$3000 K) on the nightside and relative efficient heat redistribution.
7. More realistic GCMs are required in the extreme parameter regime of KELT-9 b to explore the full implications of the observations on atmospheric drag and magnetic fields.

We highlight the power of such high-resolution phase-curve observations for directly probing atmospheric winds and thermal and chemical structures in hot Jupiters. The presented KELT-9 b data are invaluable for benchmarking 3D circulation models and developing new retrieval techniques to map out the winds. With the increasing sample of UHJs characterized by high-resolution transmission and emission spectroscopy, the emerging population-level trend will allow us to answer fundamental questions about the circulations, climates, and magnetic fields of highly irradiated exoplanets.

Acknowledgments

We thank the KPF Community Cadence observing team for their support in the observations. We thank the referee and editors for their constructive comments. We thank Ignas Snellen for helpful discussion. Y.Z. acknowledges the support from the Heising–Simons Foundation 51 Pegasi b Fellowship (grant #2023-4298). The computation was carried out on the Caltech High-Performance Cluster. J.P.W. acknowledges support from the Trottier Family Foundation via the Trottier Postdoctoral Fellowship, as well as support from the Canadian Space Agency (CSA) under grant 24JWGO3A-03. A.H. is supported by the National Science Foundation Graduate Research Fellowship under grant No. 2141064 and the MIT Dean of Science Fellowship. L.P. acknowledges support from the INAF Mini-Grant 2023 "Atmospheric structure, dynamics, and composition of hot gas-giant exoplanets with high dispersion emission spectroscopy" (PI: L. Pino).

Facility: Keck:I/KPF.

Software: `numpy` (C. R. Harris et al. 2020), `scipy` (P. Virtanen et al. 2020), `matplotlib` (J. D. Hunter 2007), `astropy` (Astropy Collaboration et al. 2013, 2018, 2022), `petitRADTRANS` (P. Mollière et al. 2019), `PyMultiNest` (J. Buchner et al. 2014), `corner` (D. Foreman-Mackey 2016).

Appendix A
The KELT-9 System

KELT-9 b is the hottest exoplanet ($T_{\rm eq} \sim 4000$ K) discovered to date (B. S. Gaudi et al. 2017). It has a 1.48 days, nearly polar orbit around an A0 star (B. S. Gaudi et al. 2017; J. P. Ahlers et al. 2020). At such a high temperature, its atmospheric chemistry resembles a dwarf star, with neutral and ionized metal species, accessible with high-resolution spectroscopy in the optical (D. Kitzmann et al. 2018; J. D. Lothringer et al. 2018). KELT-9 b features the largest number of atomic species detected in an exoplanet atmosphere

to date, such as H I, Fe I, Fe II, Ti I, Ti II, Ca I, Ca II, Mg I, Si I, O I, and many more (H. J. Hoeijmakers et al. 2018; F. Yan & T. Henning 2018; P. W. Cauley et al. 2019; F. Yan et al. 2019; J. D. Turner et al. 2020; A. Wyttenbach et al. 2020; F. Borsa et al. 2021b; A. P. Asnodkar et al. 2022; A. Bello-Arufe et al. 2022; A. B. Langeveld et al. 2022; A. Sánchez-López et al. 2022; N. W. Borsato et al. 2023, 2024; N. Lowson et al. 2023; M. C. D'Arpa et al. 2024; M. Stangret et al. 2024).

The presence of day-to-night winds in KELT-9 b has been under debate in the literature. H. J. Hoeijmakers et al. (2019) report no blueshifts of the transmission signals, while A. P. Asnodkar et al. (2022) update the ephemeris and report blueshifts due to winds up to $\sim$10 km s^{-1} (see also M. C. D'Arpa et al. 2024; M. Stangret et al. 2024). The discrepancy mainly originates from the choice of ephemeris, the instrument RV zero-points, and uncertainties in the systemic and orbital velocities. As a result of the host star's rapid rotation ($v \sin i \sim$ 115 km s^{-1}; M. Kama et al. 2023), the orbital properties and planet mass are challenging to constrain from high-resolution spectroscopy and RV measurements. Various studies, using different instruments, spectral lines, or analysis methods, report different values—the systemic velocity $v_{\rm sys}$ varies from -21.6 ± 0.8 to -17.7 ± 0.1 km s^{-1}; the orbital velocity $K_{\rm p}$ ranges from 234 ± 1 to 269 ± 6 km s^{-1}; the stellar mass ranges from 1.98 ± 0.02 to $2.32 \pm 0.16 M_{\odot}$; and the planet mass ranges from 2.17 ± 0.56 to $2.88 \pm 0.35 M_{\rm Jup}$ in the literature (F. Borsa et al. 2019; H. J. Hoeijmakers et al. 2019; A. Pai Asnodkar et al. 2022). These uncertainties limit our ability to characterize the subtle effects from atmospheric dynamics.

In addition to absorption in transmission, Fe I, Fe II, Ti I, Ti II, Ca II, Mg I, and Si I emission from the dayside has been detected, confirming the inverted temperature structure (L. Pino et al. 2020, 2022; D. H. Kasper et al. 2021; A. Ridden-Harper et al. 2023). Secondary eclipse observations using the Hubble Space Telescope's Wide Field Camera 3 show a turnoff at 1.4 μm that has been attributed either to TiO, VO, and FeH (Q. Changeat & B. Edwards 2021) or to strong absorption by H$^-$ that points to a high metallicity or a high ionization fraction whose origin remain elusive (B. Jacobs et al. 2022). However, ground-based observations find no evidence of these molecules (A. Y. Kesseli et al. 2020; D. H. Kasper et al. 2021; Y. Hayashi et al. 2024). Phase-curve observations from space, including Spitzer (M. Mansfield et al. 2020), TESS (I. Wong et al. 2020), and CHEOPS (K. Jones et al. 2022), suggest brightness temperatures at the dayside and nightside of $\sim$4500 and $\sim$3000 K, respectively. This relatively shallow temperature contrast indicates a high day-to-night heat redistribution efficiency of $\epsilon \sim 0.3$–0.5, in comparison to typical UHJs with $\epsilon < 0.1$ (L. Dang et al. 2025). The dissociation and recombination of molecular hydrogen has been invoked to explain the enhanced energy transport (T. J. Bell & N. B. Cowan 2018; M. Mansfield et al. 2020). Using high-resolution emission spectroscopy, L. Pino et al. (2022) find a deviation of the planetary RV from a circular orbit, likely caused by day-to-night atmospheric winds. Such studies with large phase coverage provide an avenue for breaking the degeneracies between the orbital motion and atmospheric winds in transmission observations.

Appendix B
Telluric Correction

We use the ESO sky tool `molecfit` to correct for telluric features in individual exposures. It uses a line-by-line radiative transfer model to derive telluric transmission spectra that can best fit the observations. The fitting parameters include the molecular abundances of telluric H_2O and O_2, the instrument resolution (modeled with a Gaussian kernel), and the continuum level of each spectral order (modeled by third-order polynomials). We perform fitting in the following wavelength regions: [6867, 6933], [7185, 7258], [7570, 7720], and [8137, 8348] Å, covering the main O_2 and H_2O bands. The wavelength solution is fixed to that of the KPF data. The relative χ^2 and parameter convergence criteria are set to 10^{-10}.

Appendix C
Supplementary Plots

We show the template spectra for various species used for the cross-correlation analysis in Figure 9.

We present the CCF map before correcting for the stellar pulsation with GP in Figure 10. The stellar contamination overlays the planetary emission signal for orbital phases $\phi < 0.1$ and $\phi > 0.4$.

With the GCM presented in Section 5.1, we find that the zonal winds across the dayside hemisphere can be well described by a sinusoidal function of longitude, as shown in Figure 11.

Finally, we show the full corner plot of our retrieval analysis in Figure 12.

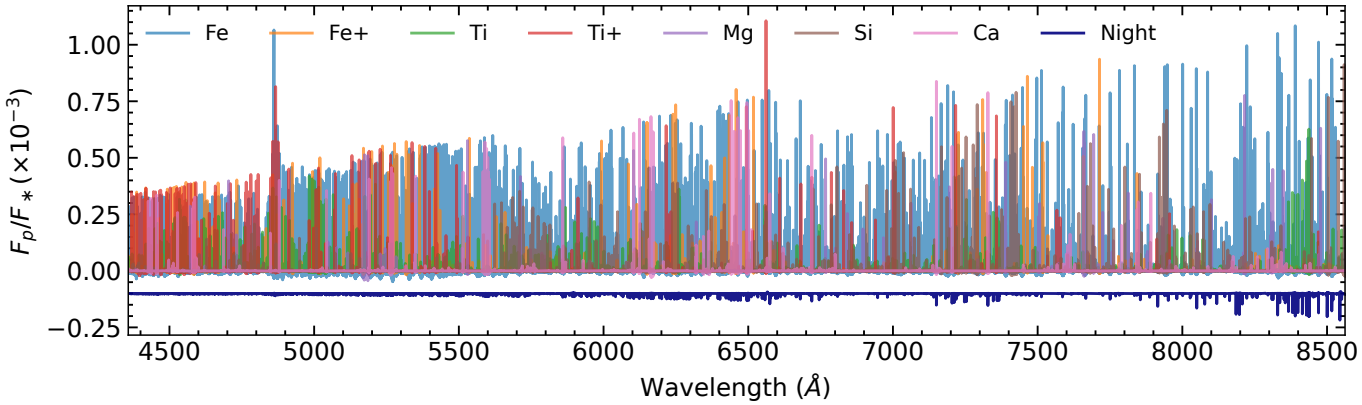

Figure 9. High-pass-filtered spectral templates of individual species used in cross-correlation analyses. The models are generated with the best-fit parameters from the retrievals (Section 3.3). The navy line shows a nightside model spectrum with all species for comparison.

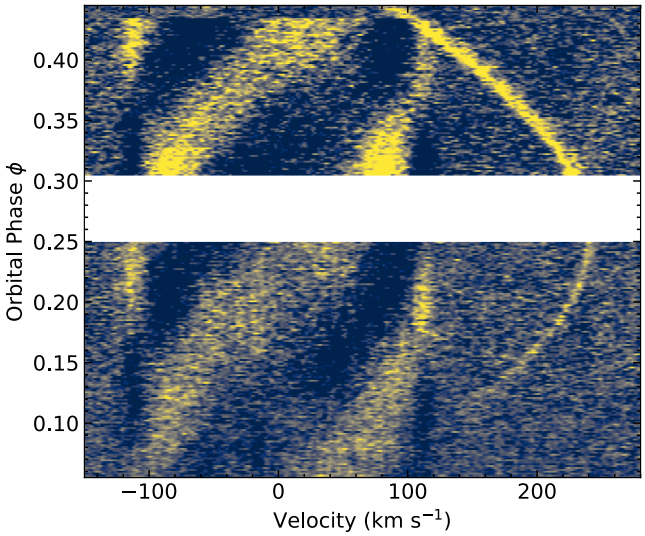

Figure 10. The same as the CCF map in Figure 1 but before the correction for the stellar pulsation pattern.

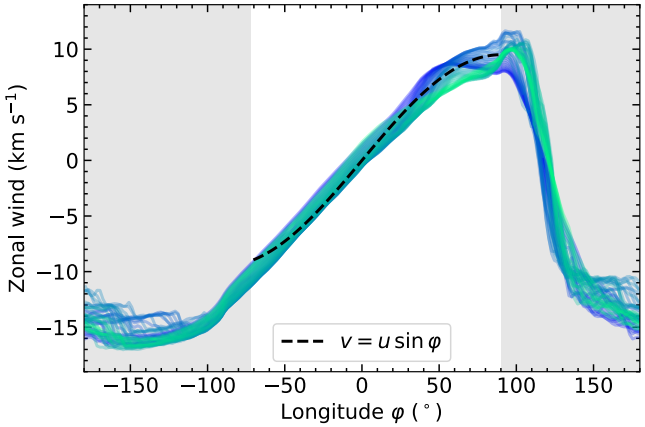

Figure 11. Zonal wind speed across longitudes from the GCM result with $\tau_{\rm drag} = 10^7$ s. The colored lines represent various latitudes between ±45°. The gray shaded region represents the nightside longitudes, while the white region represents the dayside longitudes ($-70° < \varphi < 90°$) covered by the observed phases. The black dashed line shows a sinusoidal curve that well represents the wind pattern predictions from GCMs. This also justifies our parameterization of the winds in Section 3.3.

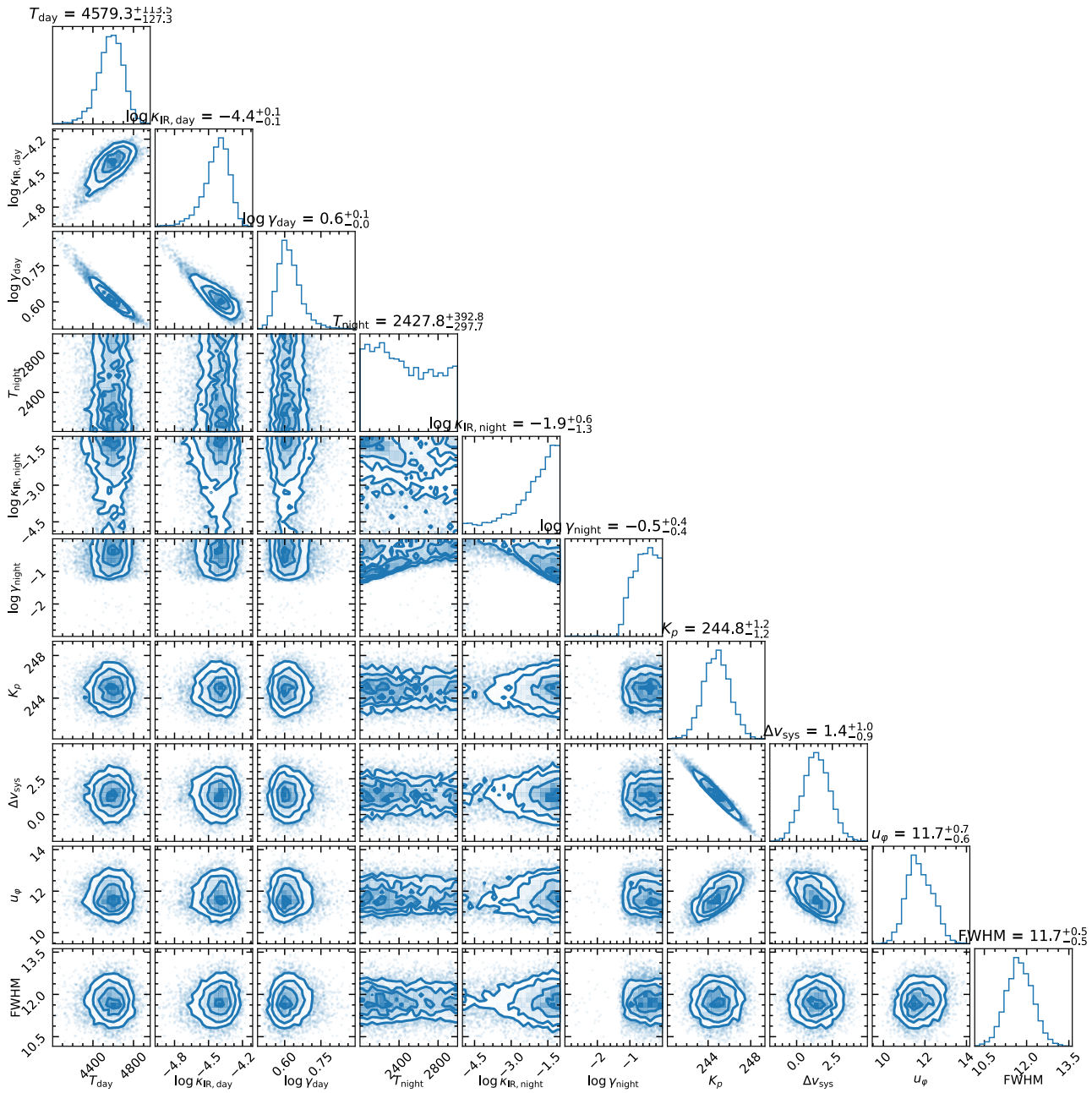

Figure 12. Corner plot of retrieved posterior distributions of parameters as listed in Table 1. The median values and 1σ uncertainties are summarized on the tops.

ORCID iDs

Yapeng Zhang https://orcid.org/0000-0003-0097-4414
Joost P. Wardenier https://orcid.org/0000-0003-3191-2486
Aaron Householder https://orcid.org/0000-0002-5812-3236
Thaddeus D. Komacek https://orcid.org/0000-0002-9258-5311
Aurora Y. Kesseli https://orcid.org/0000-0002-3239-5989
Fei Dai https://orcid.org/0000-0002-8958-0683
Andrew W. Howard https://orcid.org/0000-0001-8638-0320
Julie Inglis https://orcid.org/0000-0001-9164-7966
Howard Isaacson https://orcid.org/0000-0002-0531-1073
Heather A. Knutson https://orcid.org/0000-0002-5375-4725
Dimitri Mawet https://orcid.org/0000-0002-8895-4735
Lorenzo Pino https://orcid.org/0000-0002-1321-8856
Nicole Wallack https://orcid.org/0000-0003-0354-0187
Jerry W. Xuan https://orcid.org/0000-0002-6618-1137
Theron W. Carmichael https://orcid.org/0000-0001-6416-1274
Daniel Huber https://orcid.org/0000-0001-8832-4488
Rena A. Lee https://orcid.org/0000-0001-7058-4134
Nicholas Saunders https://orcid.org/0000-0003-2657-3889
Lauren Weiss https://orcid.org/0000-0002-3725-3058
Jingwen Zhang https://orcid.org/0000-0002-2696-2406

References

Ahlers, J. P., Johnson, M. C., Stassun, K. G., et al. 2020, AJ, 160, 4
Arcangeli, J., Désert, J.-M., Parmentier, V., et al. 2019, A&A, 625, A136
Asnodkar, A. P., Wang, J., Eastman, J. D., et al. 2022, AJ, 163, 155
Astropy Collaboration, Price-Whelan, A. M., Lim, P. L., et al. 2022, ApJ, 935, 167

Astropy Collaboration, Price-Whelan, A. M., Sipőcz, B. M., et al. 2018, AJ, 156, 123
Astropy Collaboration, Robitaille, T. P., Tollerud, E. J., et al. 2013, A&A, 558, A33
Batygin, K., Stanley, S., & Stevenson, D. J. 2013, ApJ, 776, 53
Bell, T. J., & Cowan, N. B. 2018, ApJL, 857, L20
Bell, T. J., Dang, L., Cowan, N. B., et al. 2021, MNRAS, 504, 3316
Bello-Arufe, A., Buchhave, L. A., Mendonça, J. M., et al. 2022, A&A, 662, A51
Beltz, H., & Rauscher, E. 2024, ApJ, 976, 32
Beltz, H., Rauscher, E., Roman, M. T., & Guilliat, A. 2022, AJ, 163, 35
Borsa, F., Allart, R., Casasayas-Barris, N., et al. 2021a, A&A, 645, A24
Borsa, F., Fossati, L., Koskinen, T., Young, M. E., & Shulyak, D. 2021b, NatAs, 6, 226
Borsa, F., Rainer, M., Bonomo, A. S., et al. 2019, A&A, 631, A34
Borsato, N. W., Hoeijmakers, H. J., Cont, D., et al. 2024, A&A, 683, A98
Borsato, N. W., Hoeijmakers, H. J., Prinoth, B., et al. 2023, A&A, 673, A158
Brogi, M., Emeka-Okafor, V., Line, M. R., et al. 2023, AJ, 165, 91
Brogi, M., & Line, M. R. 2019, AJ, 157, 114
Brogi, M., Snellen, I. A. G., de Kok, R. J., et al. 2012, Natur, 486, 502
Buchner, J., Georgakakis, A., Nandra, K., et al. 2014, A&A, 564, A125
Cauley, P. W., Shkolnik, E. L., Ilyin, I., et al. 2019, AJ, 157, 69
Changeat, Q., & Edwards, B. 2021, ApJL, 907, L22
Costa Silva, A. R., Demangeon, O. D. S., Santos, N. C., et al. 2024, A&A, 689, A8
Cowan, N. B., & Agol, E. 2008, ApJL, 678, L129
Dang, L., Bell, T. J., Ying, et al. 2025, AJ, 169, 32
D'Arpa, M. C., Saba, A., Borsa, F., et al. 2024, A&A, 690, A237
de Regt, S., Gandhi, S., Siebenaler, L., & González Picos, D. 2025, arXiv:2510.20870
Dietrich, W., Kumar, S., Poser, A. J., et al. 2022, MNRAS, 517, 3113
Dorn, R. J., Bristow, P., Smoker, J. V., et al. 2023, A&A, 671, A24
Ehrenreich, D., Lovis, C., Allart, R., et al. 2020, Natur, 580, 597
Feroz, F., Hobson, M. P., & Bridges, M. 2009, MNRAS, 398, 1601
Foreman-Mackey, D. 2016, JOSS, 1, 24
Foreman-Mackey, D., Yu, W., Yadav, S., et al., 2024 dfm/tinygp: The tiniest of Gaussian Process libraries, v0.3.0, Zenodo, doi:10.5281/zenodo.10463641
Fossati, L., Young, M. E., Shulyak, D., et al. 2021, A&A, 653, A52
Fromang, S., Leconte, J., & Heng, K. 2016, A&A, 591, A144
Gandhi, S., Kesseli, A., Zhang, Y., et al. 2023, AJ, 165, 242
Gaudi, B. S., Stassun, K. G., Collins, K. A., et al. 2017, Natur, 546, 514
Gibson, N. P., Merritt, S., Nugroho, S. K., et al. 2020a, MNRAS, 493, 2215
Gibson, S. R., Howard, A. W., Marcy, G. W., et al. 2016, SPIE, 9908, 2093
Gibson, S. R., Howard, A. W., Rider, K., et al. 2020b, SPIE, 11447, 848
Gibson, S. R., Howard, A. W., Rider, K., et al. 2024, SPIE, 13096, 1309609
Gibson, S. R., Howard, A. W., Roy, A., et al. 2018, SPIE, 10702, 1778
Guillot, T. 2010, A&A, 520, A27
Guilluy, G., Giacobbe, P., Brogi, M., et al. 2025, A&A, 701, A261
Harris, C. R., Millman, K. J., van der Walt, S. J., et al. 2020, Natur, 585, 357
Hayashi, Y., Narita, N., Fukui, A., et al. 2024, PASJ, 76, 1131
Herman, M. K., de Mooij, E. J. W., Nugroho, S. K., Gibson, N. P., & Jayawardhana, R. 2022, AJ, 163, 248
Hindle, A. W., Bushby, P. J., & Rogers, T. M. 2021, ApJL, 916, L8
Hoeijmakers, H. J., Ehrenreich, D., Heng, K., et al. 2018, Natur, 560, 453
Hoeijmakers, H. J., Ehrenreich, D., Kitzmann, D., et al. 2019, A&A, 627, A165
Hoeijmakers, H. J., Kitzmann, D., Morris, B. M., et al. 2024, A&A, 685, A139
Householder, A., Dai, F., Kesseli, A., et al. 2025, arXiv:2511.14175
Hunter, J. D. 2007, CSE, 9, 90
Husser, T. O., Wende-von Berg, S., Dreizler, S., et al. 2013, A&A, 553, A6
Jacobs, B., Désert, J.-M., Pino, L., et al. 2022, A&A, 668, L1
Jones, K., Morris, B. M., Demory, B. O., et al. 2022, A&A, 666, A118
Kama, M., Folsom, C. P., Jermyn, A. S., & Teske, J. K. 2023, MNRAS, 518, 3116
Kasper, D. H., Bean, J. L., Line, M. R., et al. 2021, ApJL, 921, L18
Kesseli, A. Y., Beltz, H., Rauscher, E., & Snellen, I. A. G. 2024, ApJ, 975, 9
Kesseli, A. Y., & Snellen, I. A. G. 2021, ApJL, 908, L17
Kesseli, A. Y., Snellen, I. A. G., Alonso-Floriano, F. J., Mollière, P., & Serindag, D. B. 2020, ApJ, 160, 228
Kesseli, A. Y., Snellen, I. A. G., Casasayas-Barris, N., Mollière, P., & Sánchez-López, A. 2022, ApJ, 163, 107
Kitzmann, D., Heng, K., Rimmer, P. B., et al. 2018, ApJ, 863, 183
Knutson, H. A., Charbonneau, D., Allen, L. E., et al. 2007, Natur, 447, 183
Kokori, A., Tsiaras, A., Edwards, B., et al. 2023, ApJS, 265, 4
Komacek, T. D., & Showman, A. P. 2016, ApJ, 821, 16
Komacek, T. D., Showman, A. P., & Tan, X. 2017, ApJ, 835, 198
Kreidberg, L., Line, M. R., Parmentier, V., et al. 2018, AJ, 156, 17
Kurucz, R. L. 2018, ASPC, 515, 47
Langeveld, A. B., Madhusudhan, N., & Cabot, S. H. C. 2022, MNRAS, 514, 5192
Lee, E. K. H., Wardenier, J. P., Prinoth, B., et al. 2022, ApJ, 929, 180
Lei, E., & Mollière, P. 2025, JOSS, 10, 7712
Lesjak, F., Nortmann, L., Cont, D., et al. 2025, A&A, 693, A72
Lothringer, J. D., Barman, T., & Koskinen, T. 2018, ApJ, 866, 27
Lowson, N., Zhou, G., Wright, D. J., et al. 2023, AJ, 165, 101
Mansfield, M., Bean, J. L., Stevenson, K. B., et al. 2020, ApJL, 888, L15
Mawet, D., Fitzgerald, M., Konopacky, Q., et al. 2019, BAAS, 51, 134
Mollière, P., Wardenier, J. P., van Boekel, R., et al. 2019, AJ, 627, A67
Nugroho, S. K., Gibson, N. P., de Mooij, E. J. W., et al. 2020, ApJL, 898, L31
Oh, H., Park, C., Kim, S., et al. 2024, SPIE, 13096, 90
Pai Asnodkar, A., Wang, J., Gaudi, B. S., et al. 2022, AJ, 163, 40
Parmentier, V., Line, M. R., Bean, J. L., et al. 2018, A&A, 617, A110
Pelletier, S., Benneke, B., Chachan, Y., et al. 2025, AJ, 169, 10
Pepe, F., Cristiani, S., Rebolo, R., et al. 2021, A&A, 645, A96
Perna, R., Menou, K., & Rauscher, E. 2010, ApJ, 719, 1421
Pino, L., Brogi, M., Désert, J. M., et al. 2022, A&A, 668, A176
Pino, L., Désert, J.-M., Brogi, M., et al. 2020, ApJL, 894, L27
Prinoth, B., Hoeijmakers, H. J., Kitzmann, D., et al. 2022, NatAs, 6, 449
Prinoth, B., Hoeijmakers, H. J., Morris, B. M., et al. 2024, A&A, 685, A60
Prinoth, B., Hoeijmakers, H. J., Pelletier, S., et al. 2023, A&A, 678, A182
Prinoth, B., Seidel, J. V., Hoeijmakers, H. J., et al. 2025, A&A, 694, A284
Rauscher, E., & Menou, K. 2012, ApJ, 750, 96
Ridden-Harper, A., de Mooij, E., Jayawardhana, R., et al. 2023, AJ, 165, 211
Rogers, T. M., & Komacek, T. D. 2014, ApJ, 794, 132
Sánchez-López, A., Lin, L., Snellen, I. a. G., et al. 2022, A&A, 666, L1
Savel, A. B., Beltz, H., Komacek, T. D., Tsai, S.-M., & Kempton, E. M.-R. 2024, ApJL, 969, L27
Savel, A. B., Kempton, E. M. R., Malik, M., et al. 2022, ApJ, 926, 85
Seidel, J. V., Prinoth, B., Knudstrup, E., et al. 2023, A&A, 678, A150
Seidel, J. V., Prinoth, B., Pino, L., et al. 2025, Natur, 639, 902
Seifahrt, A., Stürmer, J., Bean, J. L., & Schwab, C. 2018, SPIE, 10702, 1930
Showman, A. P., Fortney, J. J., Lewis, N. K., & Shabram, M. 2013, ApJ, 762, 24
Sing, D. K., Evans-Soma, T. M., Rustamkulov, Z., et al. 2024, AJ, 168, 231
Smette, A., Sana, H., Noll, S., et al. 2015, A&A, 576, A77
Snellen, I. 2025, ARA&A, 63, 83
Spiegel, D. S., Silverio, K., & Burrows, A. 2009, ApJ, 699, 1487
Stangret, M., Fossati, L., D'Arpa, M. C., et al. 2024, A&A, 692, A76
Stevenson, K., Lothringer, J. D., Beltz, H., et al. 2025, JWST Proposal, Cycle 4, 7255
Tan, X., & Komacek, T. D. 2019, ApJ, 886, 26
Turner, J. D., de Mooij, E. J. W., Jayawardhana, R., et al. 2020, ApJL, 888, L13
van Sluijs, L., Birkby, J. L., Lothringer, J., et al. 2023, MNRAS, 522, 2145
Virtanen, P., Gommers, R., Oliphant, T. E., et al. 2020, NatMe, 17, 261
Wardenier, J. P., Parmentier, V., Lee, E. K. H., & Line, M. R. 2025, ApJ, 986, 63
Wardenier, J. P., Parmentier, V., Lee, E. K. H., Line, M. R., & Gharib-Nezhad, E. 2021, MNRAS, 506, 1258
Wardenier, J. P., Parmentier, V., Line, M. R., et al. 2024, PASP, 136, 084403
Wong, I., Shporer, A., Kitzmann, D., et al. 2020, AJ, 160, 88
Wyttenbach, A., Mollière, P., Ehrenreich, D., et al. 2020, A&A, 638, A87
Xuan, J. W., Wang, J., Ruffio, J.-B., et al. 2022, ApJ, 937, 54
Yan, F., Casasayas-Barris, N., Molaverdikhani, K., et al. 2019, A&A, 632, A69
Yan, F., & Henning, T. 2018, NatAs, 2, 714
Yan, F., Pallé, E., Reiners, A., et al. 2020, A&A, 640, L5
Zhang, J., Kempton, E. M.-R., & Rauscher, E. 2017, ApJ, 851, 84
Zhang, Y., Picos, D. G., de Regt, S., et al. 2024, AJ, 168, 246
Zhang, Y., Snellen, I. A. G., Wyttenbach, A., et al. 2022, A&A, 666, A47